Simulation of gas flow through tubes of finite length over the whole range of rarefaction for various pressure drop ratios

S. Varoutis[a)] and D. Valougeorgis
*Department of Mechanical and Industrial Engineering, University of Thessaly, Pedion Areos,
Volos 38334, Greece*

F. Sharipov
Departamento de Física, Universidade Federal do Paraná, Caixa Postal 19044, Curitiba 81531-990, Brazil

The rarefied gas flow through circular tubes of finite length has been investigated computationally by the direct simulation Monte Carlo method. The reduced flow rate and the flow field have been calculated as functions of the gas rarefaction, the length-to-radius ratio, and the pressure ratio along the tube. The gas rarefaction, which is inversely proportional to the Knudsen number, is varied from 0 to 2000, i.e., the free-molecular, transitional, and hydrodynamic regimes are embraced. A wide range of the length-to-radius ratio, namely, from 0 corresponding to the orifice flow up to 10 representing a sufficiently long tube, has been considered. Several values of the pressure ratio between 0 and 0.7 have been regarded. This pressure range covers both gas flow into vacuum and into a background gas. It has been found that the rarefaction parameter has the most significant effect on the flowfield characteristics and patterns, followed by the pressure ratio drop, while the length-to-radius ratio has a rather modest impact. Several interesting findings have been reported including the behavior of the flow rate and other macroscopic quantities in terms of these three parameters. In addition, the effect of gas rarefaction on the choked flow and on the Mach disks at large pressure drops is discussed. Comparison of some of the present numerical results with available experimental data has shown a good agreement. © *2009 American Vacuum Society.*
[DOI: 10.1116/1.3248273]

I. INTRODUCTION

The detailed quantitative description of the flow field of rarefied gas flows through short circular tubes is of major importance in the optimized design and operation of various types of industrial equipment in several technological fields. Some of these applications may include mass flow controllers in gas metering, micropropulsion in high altitude and space gas dynamics, pipe networks, pumps and distillation towers in vacuum systems, membranes and porous media in filtering, fabrication processes in microelectronics, and gaseous devices in microelectromechanical systems. It is noted that in all these applications the operation of the system may be under low, medium, or high vacuum conditions.

Due to its theoretical and practical importance, this flow has been extensively investigated. Following the pioneering work by Knudsen[1] and Clausing,[2] many studies, both theoretical and experimental, on flows through orifices and short tubes have been reported. A list of all these works would be too lengthy to report here, and thus we cite only some of them, which are more related to the present work.[3–7] Also, a more complete and detailed bibliographic review may be found in Refs. [8–10].

The flow of rarefied gases between two reservoirs through short tubes, despite its simple geometry, requires significant computational effort, mainly due to the fact that large regions in both reservoirs must be included in the simulation to allow an accurate description of the flow field. The most common computational scheme to handle this type of flow in the transition regime is the direct simulation Monte Carlo (DSMC) method described in Ref. [11], while in the slip and hydrodynamic regimes, the compressible Navier–Stokes equations with slip and no-slip boundary conditions, respectively, may be applied. It is noted that although, in general, the DSMC approach is very efficient, the computational effort becomes very demanding particularly when all geometric and flow parameters, which may influence the flow, are examined. The most computationally expensive cases occur when the length-to-radius ratio is increased and the pressure drop is small, but still the flow may not be considered as fully developed and cannot be handled by linearized kinetic theory or both. In addition, the required computational time and storage are increased as the Knudsen number is decreased. It is also noted that very few experimental works cover the whole range of the involved parameters. Therefore, even though the subject has been studied for a long time, the available data needed for engineering purposes are still limited.

In that framework the conductance of nitrogen gas through circular tubes of various length-to-diameter ratios and for several pressure ratios along the tube have been computed and measured.[12,13] Both experimental and computational conductances were found to be lower than the ones provided in Ref. [3]. In Ref. [12] the authors also proposed an expression to estimate conductance in the continuum regime and in the transition regime at small Knudsen numbers. In

---

the case of small cylindrical sonic orifices, the dependency of the discharge coefficients on the length-to-diameter ratio and on the Reynolds number have been studied experimentally.[14] It is well known that cylindrical microtubes, while they perform as well as typical micronozzles, offer the advantage of simple manufacturing. In Ref. 14 in addition to conductance, the flow structure inside the tube has been monitored to find several compression waves inside the nozzle. In an effort to optimize the design of short tubes for aerospace propulsion, the effect of the length of thin wall orifices have studied computationally and experimentally.[15,16] This work includes two length-to-diameter ratios and flows into vacuum. It has been deduced that the thick orifice has a higher propulsion efficiency. In most of these works, the results are in dimensional form and they are related to specific gases. Recently, in Ref. 17 the DSMC algorithm has been applied to provide generalized results for the flow rate and the macroscopic distributions for tubes with several length-to-radius ratios. However, again as in Refs. 15 and 16, the flow is expanding into vacuum; i.e., the background gas pressure equals to zero. A detailed experimental work has been recently performed for long and short tubes, covering the whole range of Knudsen number.[18] The experimental data have been compared with the corresponding numerical data available in the literature including the computational results by Varoutis *et al.*,[17] for gas flows through short tubes into vacuum, where a very good agreement has been observed.

As it is seen although significant amount of work has been performed, there is no computational study so far, providing results in a wide range of all involved flow and geometric parameters. In the present work, based on the DSMC approach, the flow of a monoatomic gas through circular tubes with length-to-radius ratios from 0 to 10 and the downstream over the upstream pressure ratio ranging from 0.1 up to 0.7 is numerically investigated. Since the dependency of the results on the gas-surface interaction law and on the intermolecular potential have been studied before,[17] here we apply only the diffuse scattering and the hard sphere model for gaseous molecules and focus our investigation on the effects of the rarefaction, the pressure drop, and the tube length on the flow quantities and characteristics. Numerical results for the flow rate and the macroscopic distributions of the flow (velocity, pressure, and temperature) are presented in the whole range of the Knudsen number and in reasonably wide ranges of the length-to-radius and pressure ratios. All results are reported in dimensionless form in order to be general and easily adapted to specific flow conditions. For certain flow configurations, the numerical results are compared successfully with corresponding experimental results in Refs. 4 and 6. Note that it is the first time that mass flow rate and flow field are calculated in the whole range of gas rarefaction and wide range of length-to-radius ratios and pressure drops.

II. STATEMENT OF THE PROBLEM

Consider the axisymmetric flow of a monoatomic gas through a tube of radius R and finite length L, connecting
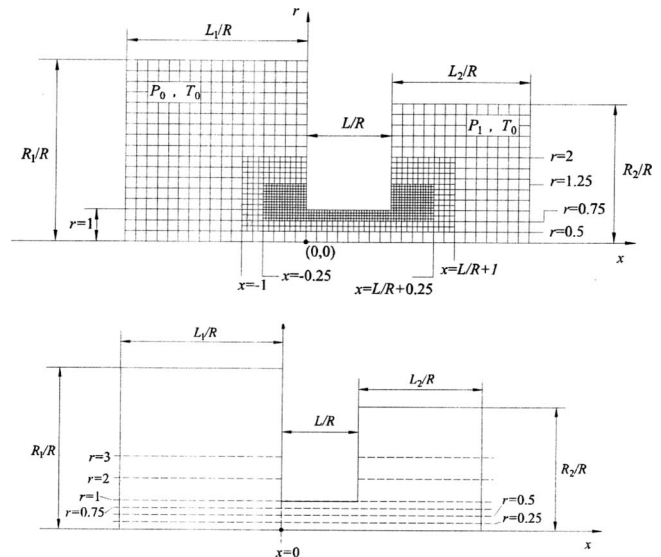

FIG. 1. Geometry and three-level computational domain (top). Weighting zones (bottom).

two semi-infinite reservoirs, maintained at pressures P_0 and P_1 ($P_0 > P_1$). The geometric configuration with the coordinate system (x, r) and its origin are shown in Fig. 1. The upstream and downstream reservoirs, in Fig. 1, are shown having finite volumes due to computational restrictions. The temperature in the reservoirs far from the inlet and outlet of the tube as well as along the tube walls and the plates at $x=0$ and $x=L/R$ is kept constant and equal to T_0. The quantities n_0, P_0, and T_0 are taken as reference density, pressure, and temperature, respectively, with $P_0 = n_0 k T_0$, while k denotes the Boltzmann constant.

The solution of this flow configuration is determined in terms of three parameters, namely, the length-to-radius ratio L/R of the tube, the pressure ratio P_1/P_0, and the reference rarefaction parameter, defined as, see, e.g., Ref. 8:

$$\delta = \frac{RP_0}{\mu_0 v_0}, \tag{1}$$

where μ_0 is the gas viscosity at T_0 and $v_0 = \sqrt{2kT_0/m}$ is the most probable molecular speed with m denoting the molecular mass of the gas. The radius R and the velocity v_0 are taken as the characteristic length and velocity, respectively. It is noted that since the ratio μ_0/P_0 is proportional to the molecular mean free path, the rarefaction parameter δ is inversely proportional to the Knudsen number, i.e., $\delta \propto 1/\text{Kn}$. Hence, the limit $\delta=0$ represents the free-molecular regime, while the opposite situation, i.e., $\delta \gg 1$, corresponds to the continuum mechanics regime. The main idea of the implementation of the rarefaction parameter instead of the Knudsen number is to avoid using directly the mean free path, which is not well defined and depends on the choice of the molecular potential. Also, it is noted that the pressure ratio P_1/P_0 may vary between 0 and 1 and as it is decreased the pressure drop is increased.

The reduced flow rate W through the tube is defined as

$$W = \frac{\dot{M}}{\dot{M}_0}. \tag{2}$$

Here, $\dot{M}$ is the mass flow rate through the tube at any L/R, P_1/P_0 and δ, while

$$\dot{M}_0 = \frac{\sqrt{\pi}R^2}{v_0}P_0 \tag{3}$$

is the mass flow rate through an orifice ($L/R=0$) into vacuum ($P_1/P_0=0$) at the free molecular limit ($\delta=0$) and it is calculated analytically. Note that in the case of the free-molecular flow through a tube into vacuum, i.e., $\delta=0$ and $P_1/P_0=0$, the quantity W becomes the transmission probability, see, e.g., Refs. 8 and 11.

Over the years several empirical expressions have been derived for W, based on experimental and numerical data. Although all these equations are valid only in certain ranges of the geometric and flow parameters, they may be useful for handy calculations. Such empirical formulas are the ones proposed in Ref. 6 for flows into vacuum as well as the one proposed in Ref. 4 for the more general case of any pressure ratio:

$$W^{(S)} = \frac{1 - P_1/P_0}{1 + L/(2R)}\left[\frac{1 + P_1/P_0}{5\sqrt{\pi}}\delta + 1.038\right]. \tag{4}$$

The latter one as well as some of the experimental results in Ref. 6 for nonzero background pressure are applied in Sec. IV for comparison purposes with the present numerical results.

III. DSMC ALGORITHM

All calculations have been performed using the DSMC method, based on the no-time counterscheme, see Ref. 11. In brief, the DSMC approach may be described as follows: A sample of model molecules is evolved in time to statistically mimic the behavior of real molecules. At each time step, the process is split between streaming and collisions. The state of the system is defined by the position and velocity vectors of the model particles. Each model particle in the simulation represents a large number of real molecules in the physical system. A rigorous proof that DSMC produces a solution to the Boltzmann equation in the limit of vanishing discretization and stochastic errors has been provided in Ref. 19. The problem, due to the axisymmetry of the flow, may be considered as two dimensional in the physical space. This is achieved by rotating the velocity vector according to the procedure described in Section 15.1 of Ref. 11.

Recently, the DSMC algorithm has been accordingly modified and successfully applied to the simulation of rarefied gas flows through tubes of finite length into vacuum in Ref. 17, i.e., at $P_1/P_0=0$. Here, this code is extended to include the more general case of arbitrary pressure drops, i.e., when $P_1/P_0>0$. Since the details of the algorithm are well known and described in Ref. 11, its detailed description is omitted and only specific issues related to the present formulation are provided for completeness and clarity.

The axisymmetric computational grid, shown in Fig. 1, is structured with nonuniform cells of three different sizes. Such a three-level grid is required in order to capture the steep macroscopic gradients close to the boundaries and maintain reasonable computational efficiency. In addition, as shown in Fig. 1, three radial and seven axial weighting zones have been incorporated to ensure more uniform distributions of model particles over the computational domain, see Refs. 7 and 17. The computational parameters have been accordingly chosen to ensure results accurate up to at least 1%. In particular, in all cases, the time increment and the largest cell side of the grid are taken equal to

$$\Delta t = 0.01R/v_0 \tag{5}$$

and

$$\Delta x' = 0.05R, \tag{6}$$

respectively. Also, in all cases the number of model molecules is $N=3\times10^7$. It has been found that this number of computational particles is adequate to ensure numerical results within the prescribed error in the hydrodynamic limit and therefore in all other regimes as well. In addition, several computational sizes of the upstream and downstream reservoirs have been tested and the minimum ones, which guarantee an invariance in the results of less than 1%, have been selected. It has been found that this is achieved by taking $L_1=R_1=L_2=R_2=8R$. Finally, it is noted that the same investigation has been performed for different sizes of the computational grid and the final parameters also guarantee the invariance in the results of less than 1%.

The total number of cells is about 8×10^4 and the number of particles in each cell varies between 10^2 and 2×10^3. Finally, the evolution of the system (i.e., the number of times steps or samples) is terminated when the relative scattering of the results satisfy the condition

$$\frac{\sqrt{N^+}}{N^+ - N^-} < 0.001, \tag{7}$$

where N^+ and N^- denote the total numbers of particles crossing from left to right and from right to left, respectively, the inlet cross section of the tube at $x=0$ during the simulation time.

It is noted that the computational effort is significantly increased as the ratios P_1/P_0 and L/R are increased. This is easily justified since, at large P_1/P_0 and L/R, the quantity N^- gets closer to N^+. Therefore, the relative scattering of the flow given by Eq. (7) is increased as well. The computational effort is also increased, as the rarefaction parameter δ approaches the hydrodynamic limit because the number of the intermolecular collision to be simulated is enlarged.

Initially, the modeled particles are distributed uniformly over the left container and inside the tube with the density given by

$$n_L = \frac{n_0}{F_N}, \tag{8}$$

where $n_0 = P_0/kT_0$ is the equilibrium density in the right container and F_N is the number of real molecules represented by one model particle. The model particles in the right container are also distributed uniformly with the density given as

$$n_R = n_L \frac{P_1}{P_0}. \tag{9}$$

Then, during the streaming stage some of them are freely moved through some distance defined by the time step Δt and their velocities c_i ($1 \leq i \leq N$), while others may interact with the solid boundaries of the tube or of the reservoirs. The interaction of particles with the solid boundaries maintained at temperature T_0 is simulated by diffuse reflection. Also, during the free motion some particles may get out from the computational domain and then they are eliminated for the rest of the simulation. At the same time, new particles are generated at the open boundaries of the computational domain having the corresponding Maxwellian distributions defined by (P_0, T_0) in the left reservoir and by (P_1, T_0) in the right one. The number of particles entering the computational domain through the boundaries of the left and right containers is defined by

$$N_L = \frac{1}{2\sqrt{\pi}} A_L n_L v_0 \Delta t, \tag{10}$$

and

$$N_R = \frac{1}{2\sqrt{\pi}} A_R n_R v_0 \Delta t, \tag{11}$$

respectively. Here, A_L and A_R are the areas of the left and right open boundaries, while n_L and n_R are given by Eqs. (8) and (9), respectively. It is noted that N_L and N_R remain constant for all time intervals. Upon establishing steady state conditions the number of particles leaving and entering the computational domain is approximately the same and therefore the total number of simulated particles remains practically constant.

During the collision stage, particles within a cell are randomly selected as a collision pair according to collision probabilities derived from kinetic theory. Since it was shown, in previous works,[7,17] that the influence of the intermolecular potential model on this type of flow is modest, here we consider only the hard sphere particles with a constant cross section. Therefore, in the present work, the viscosity is proportional to $\sqrt{T}$ and the dimensionless results, presented in Sec. IV are general in the sense that they can be used for any gas.

The mass flow rate $\dot{M}$ can be expressed in terms of the net number of particles crossing the inlet of the tube at $x=0$ as

$$\dot{M} = \frac{m(N^+ - N^-)F_N}{t}, \tag{12}$$

where t is the total simulation time. Then, according to Eq. (2), the reduced flow rate W is estimated as

$$W = \frac{2}{\sqrt{\pi}} \frac{(N^+ - N^-)V}{R^2 t v_0 N}, \tag{13}$$

where V is the volume of the computational domain and N is the number of model particles generated initially.

The number density in a computational cell is given by

$$n_j = \frac{\bar{N}_j F_N}{V_j}, \quad j = 1, 2, \ldots, J, \tag{14}$$

where j denotes the computational cell having volume V_j, J is the total number of cells, and $\bar{N}_j$ is the average value of the number of particles in the jth cell at each time interval. The dimensionless number density is given as

$$\frac{n_j}{n_0} = \frac{\bar{N}_j}{N} \frac{V}{V_j}, \quad j = 1, 2, \ldots, J. \tag{15}$$

Working in a similar manner the dimensionless bulk velocity vector and temperature of the jth cell are found to be

$$\frac{u_j}{v_0} = \frac{1}{N_j} \sum_{i=1}^{N_j} c_{ij}, \quad j = 1, 2, \ldots, J \tag{16}$$

and

$$\frac{T_j}{T_0} = \frac{2}{3} \left[\frac{1}{N_j} \sum_{i=1}^{N_j} c_{ij}^2 - \left(\frac{u}{v_0} \right)^2 \right], \quad j = 1, 2, \ldots, J. \tag{17}$$

respectively. In Eqs. (16) and (17), N_j is the number of particles in the jth cell and c_{ij} denotes the dimensionless three component molecular velocity vector of the ith particle at the jth cell. Both quantities refer to the total time of the simulation. Finally, the dimensionless pressure is calculated using the equation of state as

$$\frac{P_j}{P_0} = \frac{n_j}{n_0} \frac{T_j}{T_0}, \quad j = 1, 2, \ldots, J. \tag{18}$$

In Sec. IV, the numerical results are presented for the flow rate and the distributions of velocity, pressure, and temperature.

IV. RESULTS AND DISCUSSIONS

Calculations have been carried out for the following ranges of the parameters determining the solution: $0 \leq \delta \leq 2 \times 10^3$, $0 < L/R \leq 10$, and $0 \leq P_1/P_0 \leq 0.7$. It is noted that the obtained results cover actually the whole range of δ and a reasonably wide range of L/R and P_1/P_0. For this range of parameters, the results are presented in Sec. IV A and IV B. The first one is focused on the flow rate including some comparisons with experimental results and the second one provides an analysis of the flow field.
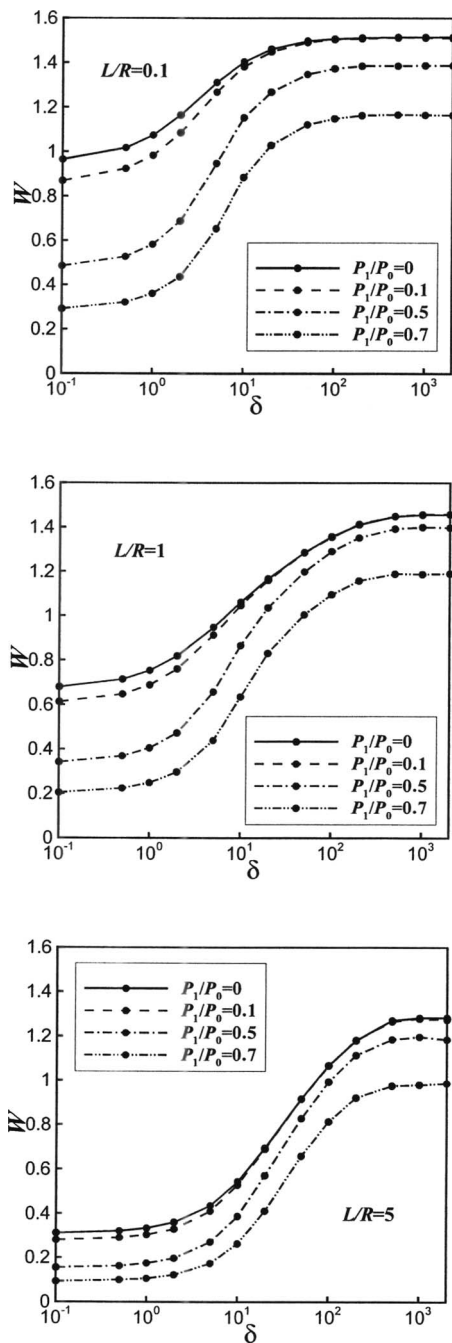
FIG. 2. Dimensionless flow rate W in terms of δ for various L/R and P_1/P_0.

FIG. 3. Dimensionless flow rate W in terms of P_1/P_0 for various L/R and δ.

A. Flow rate

The behavior of the dimensionless flow rate W in terms of the parameters δ, L/R and P_1/P_0 is shown in Figs. 2–4, respectively. In Fig. 2, the results of W with regard to the rarefaction parameter for $L/R=0.1,1,5$ and $P_1/P_0 =0,0.1,0.5,0.7$ are shown. In all cases the qualitative dependency of W on δ is similar. More specifically, as δ is increased from 0 to 1, W is increased very slowly; then in the range $1 \leqslant \delta \leqslant 10^2$ there is a significant increase of W and finally, at the large values of δ, W keeps increasing very weakly reaching asymptotically the continuum results at the
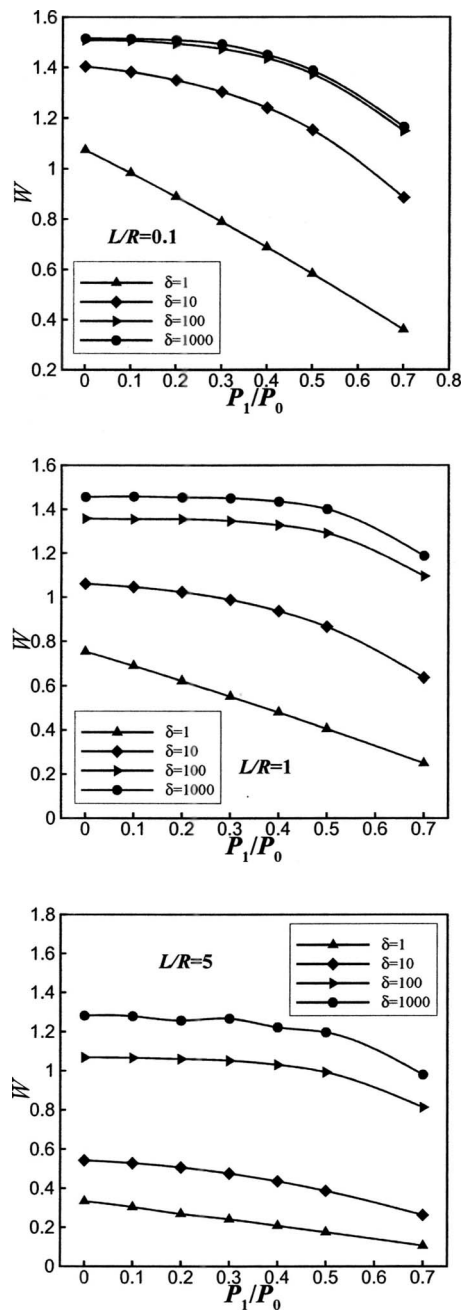
hydrodynamic limit $(\delta \rightarrow \infty)$. It is noted that the results for $P_1/P_0=0$ and 0.1 are almost identical when $\delta > 10$.

The dependency of W on P_1/P_0 for $L/R=0.1,1,5$ and $\delta =1,10,10^2,10^3$ is shown in Fig. 3. In all cases W is increased as P_1/P_0 is decreased (i.e., as the difference between upstream and downstream pressures is increased). It is seen, however, that as the pressure ratio is decreased, at small L/R and δ, W is rapidly increased, while at large L/R and δ the increase in W is modest. Actually, in some cases (e.g., $L/R =5$ and $\delta=10^2$ or 10^3), there is a critical pressure ratio $(P_1/P_0)^*$, beyond which as P_1/P_0 is further decreased the corresponding increase in W is not significant. This phenomenon, called choked flow, is well known in the continuum
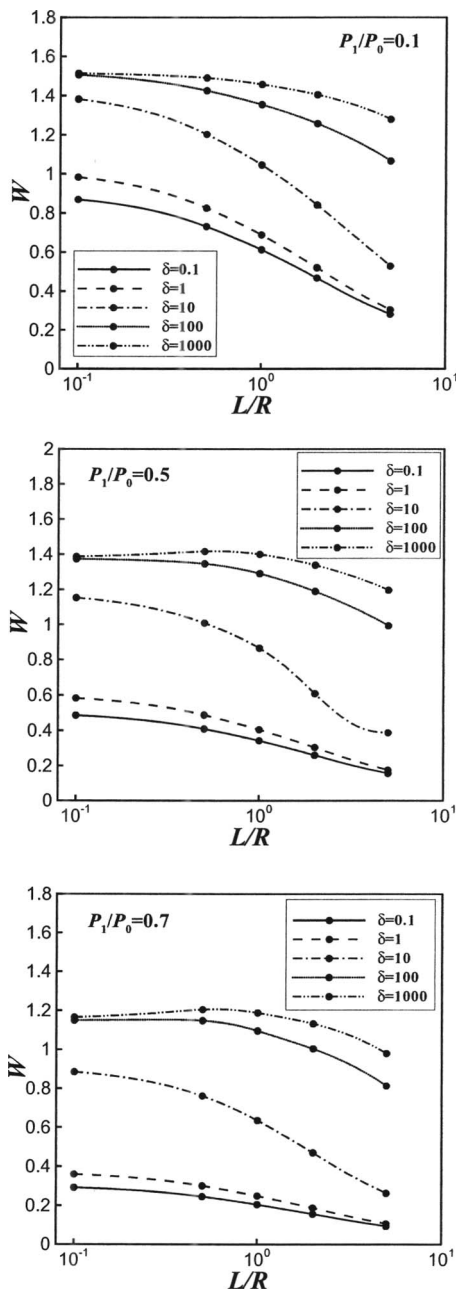
FIG. 4. Dimensionless flow rate W in terms of L/R for various P_1/P_0 and δ.
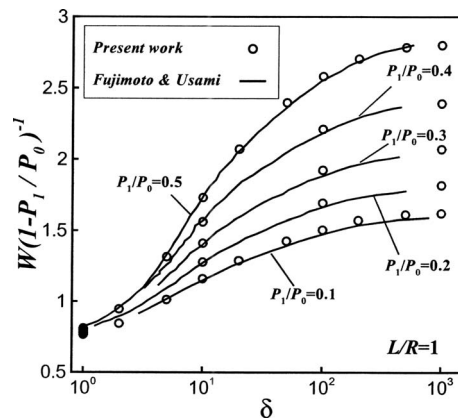

FIG. 5. Comparison between the present DSMC results and the corresponding experimental data by Fujimoto and Usami (Ref. 6).

which is present in the hydrodynamic regime, has been also observed in experimental work, see, e.g., Refs. 16 and 20 but it has not been yet physically explained.

A comparison between the present numerical results and the experimental results in Ref. 6 is performed in Fig. 5. The experimental results have been obtained by digitizing Fig. 8 in Ref. 6 for $L/R=0.99$, $\delta>1$, and $0 \leqslant P_1/P_0 \leqslant 0.5$. In order to be able to perform the comparison, the corresponding results of W for $L/R=1$, presented here, are multiplied by the quantity $(1-P_1/P_0)^{-1}$. The very good agreement between the experiment and simulation, in a wide range of δ and P_1/P_0, validates the numerical solution at $L/R=1$ and it is reasonable to expect that this accuracy is extended to other length-to-radius ratios as well.

Another comparison with experimental results is performed in Fig. 6, based on the empirical expression (4) in Ref. 4, for various set of parameters. The agreement is good in the free molecular and part of the transition regime up to $\delta \leqslant 2$ and reasonably good for $2 < \delta \leqslant 5$ and $P_1/P_0=0.7$ and 0.5. Outside this range of parameters, formula (4) is not reliable.

This subsection is closed by providing some tabulated results for the flow rate W in terms of δ and L/R in Tables I–III for $P_1/P_0=0.1$, 0.5, and 0.7, respectively. For the case of $L/R=10$, the numerical effort is very intense and therefore results are provided only for limited number of δ in the free molecular and transition regimes. Also, in Table IV, results for W are tabulated for $P_1/P_0=0.2, 0.3, 0.4$ and for characteristic values of δ and L/R. It is noted that Tables I–IV include some results presented before in graphical form and also additional results covering a wide range of all three parameters determining the flow. We consider that the tabulated results are important in this type of research work since they can be easily accessed by the research community for comparison purposes with experimental results or as benchmarks for validation of computational work.

B. Flow field

We continue with a more detailed observation inside the flow field by providing, in Fig. 7, the streamlines for

limit and it is also present in rarefied flows. It is deduced, however, that the value of the critical pressure ratio is decreased as the rarefaction is increased (i.e., by decreasing δ). It is also noted that at $L/R=0.1$, the corresponding results for $\delta=10^2$ and 10^3 almost coincide.

In Fig. 4, the results of W in terms of L/R are shown for $P_1/P_0=0.1, 0.5, 0.7$ and $\delta=10^{-1}, 1, 10, 10^2, 10^3$. As expected in most cases, W has its maximum value at $L/R=0$ and then it is decreased as the length to radius ratio is increased. It is observed, however, that for some set of parameters and, in particular, for large P_1/P_0 and δ, W may have a slight maximum at some L/R different than zero. This phenomenon,
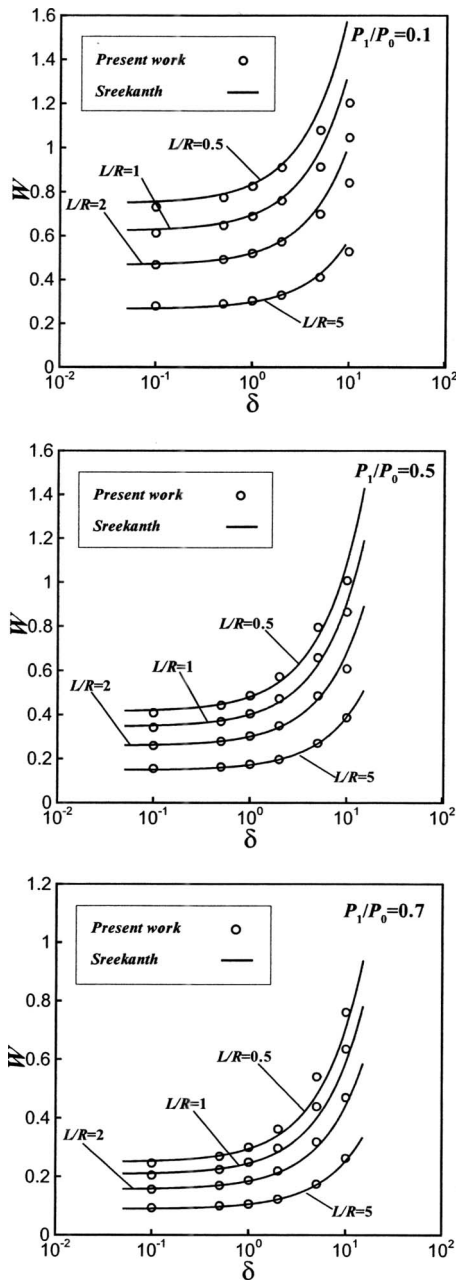
FIG. 6. Comparison between the present DSMC results and the corresponding experimental data by Sreekanth (Ref. 4).

$P_1/P_0=0.5$, $L/R=0.5,5$, and $\delta=1,10,10^2,10^3$. It is seen that in the transition regime ($\delta=1$) the streamlines are almost symmetric before and after the tube and no vortices are present. This flow pattern is typical for any pressure and length-to-radius ratios when $\delta \leq 1$. As δ is increased, the streamlines bend and vortices start to appear in the downstream reservoir. At $\delta=10$, such vortices have already been created, while at $\delta=10^2$ and 10^3, these vortices have been enlarged and as a result strong jets of gas along $r=0$ at the exit of the tube have been produced. The diameter of the jets is equal to the diameter of the tube and its length is extended downstream several L/R. Comparing the streamlines between $L/R=0.5$ and 5, it is seen that the vortex creation is

TABLE I. Dimensionless flow rate W vs L/R and δ for $P_1/P_0=0.1$.

δ	$L/R=0.1$	0.5	1	2	5	10
			W			
0	0.856	0.721	0.605	0.463	0.279	0.170
0.1	0.869	0.731	0.613	0.468	0.281	
0.5	0.924	0.775	0.648	0.493	0.291	1.171
1	0.984	0.826	0.689	0.521	0.304	
2	1.08	0.911	0.761	0.573	0.330	0.192
5	1.27	1.08	0.913	0.699	0.412	
10	1.38	1.20	1.05	0.842	0.529	0.321
20	1.45	1.29	1.16	0.985	0.689	
50	1.49	1.38	1.28	1.15	0.915	
100	1.51	1.43	1.35	1.26	1.07	
200	1.51	1.46	1.41	1.34	1.18	
500	1.51	1.48	1.45	1.39	1.27	
1000	1.51	1.49	1.46	1.40	1.28	
2000	1.51	1.49	1.46	1.40	1.27	

delayed as L/R is increased. The flow patterns, shown in Fig. 7, for $P_1/P_0=0.5$ is typical for any pressure ratio $0 \leq P_1/P_0 \leq 0.7$.

The variation in the pressure, temperature, and local Mach along the symmetry axis $r=0$ and $-4 \leq x \leq L/R+8$ are shown in Figs. 8–10, respectively, for $\delta=1$, 10, 100, and 1000, $L/R=0.1$ and 5, and $P_1/P_0=0.1$, 0.3, and 0.5.

In Fig. 8, for $\delta=1$, the pressure variation is decreased monotonically. It starts from its upstream equilibrium value P_0 and remains constant for $x \leq -2$. Then, it drops along the distance $-2 \leq x \leq L/R+2$ reaching its downstream equilibrium value P_1, which remains constant for $x > L/R+2$. The corresponding temperature in Fig. 9, for $\delta=1$, is constant and equal to its equilibrium value for $x \leq -2$, and then it starts dropping until $x \simeq L/R$, where for all L/R, it has a minimum. Next, it is increasing and reaches its equilibrium value, which is equal to T_0. In general, the temperature variation,

TABLE II. Dimensionless flow rate W vs L/R and δ for $P_1/P_0=0.5$.

δ	$L/R=0.1$	0.5	1	2	5	10
			W			
0	0.475	0.399	0.336	0.256	0.155	0.0935
0.1	0.486	0.409	0.343	0.260	0.156	
0.5	0.528	0.444	0.370	0.280	0.163	0.0934
1	0.583	0.488	0.405	0.304	0.175	
2	0.688	0.573	0.474	0.351	0.197	0.114
5	0.948	0.796	0.658	0.486	0.271	
10	1.15	1.01	0.866	0.669	0.388	0.223
20	1.27	1.15	1.04	0.864	0.571	
50	1.35	1.28	1.20	1.07	0.828	
100	1.37	1.35	1.29	1.19	0.993	
200	1.39	1.39	1.35	1.28	1.11	
500	1.39	1.41	1.39	1.32	1.18	
1000	1.39	1.42	1.40	1.34	1.20	
2000	1.39	1.42	1.40	1.34	1.19	

TABLE III. Dimensionless flow rate W vs L/R and δ for $P_1/P_0=0.7$.

δ	$L/R=0.1$	0.5	1	2	5	10
			W			
0	0.286	0.241	0.201	0.153	0.093	0.0543
0.1	0.292	0.246	0.205	0.156	0.093	
0.5	0.321	0.270	0.224	0.170	0.100	0.0606
1	0.361	0.300	0.249	0.190	0.106	
2	0.436	0.363	0.298	0.220	0.123	0.0700
5	0.654	0.541	0.440	0.319	0.174	
10	0.885	0.762	0.640	0.471	0.263	0.146
20	1.03	0.937	0.831	0.672	0.411	
50	1.12	1.08	1.00	0.884	0.658	
100	1.15	1.15	1.10	1.00	0.814	
200	1.16	1.19	1.16	1.09	0.922	
500	1.17	1.20	1.19	1.13	0.975	
1000	1.16	1.20	1.19	1.13	0.980	
2000	1.16	1.20	1.19	1.13	0.986	

TABLE IV. Dimensionless flow rate W vs L/R and δ for various P_1/P_0.

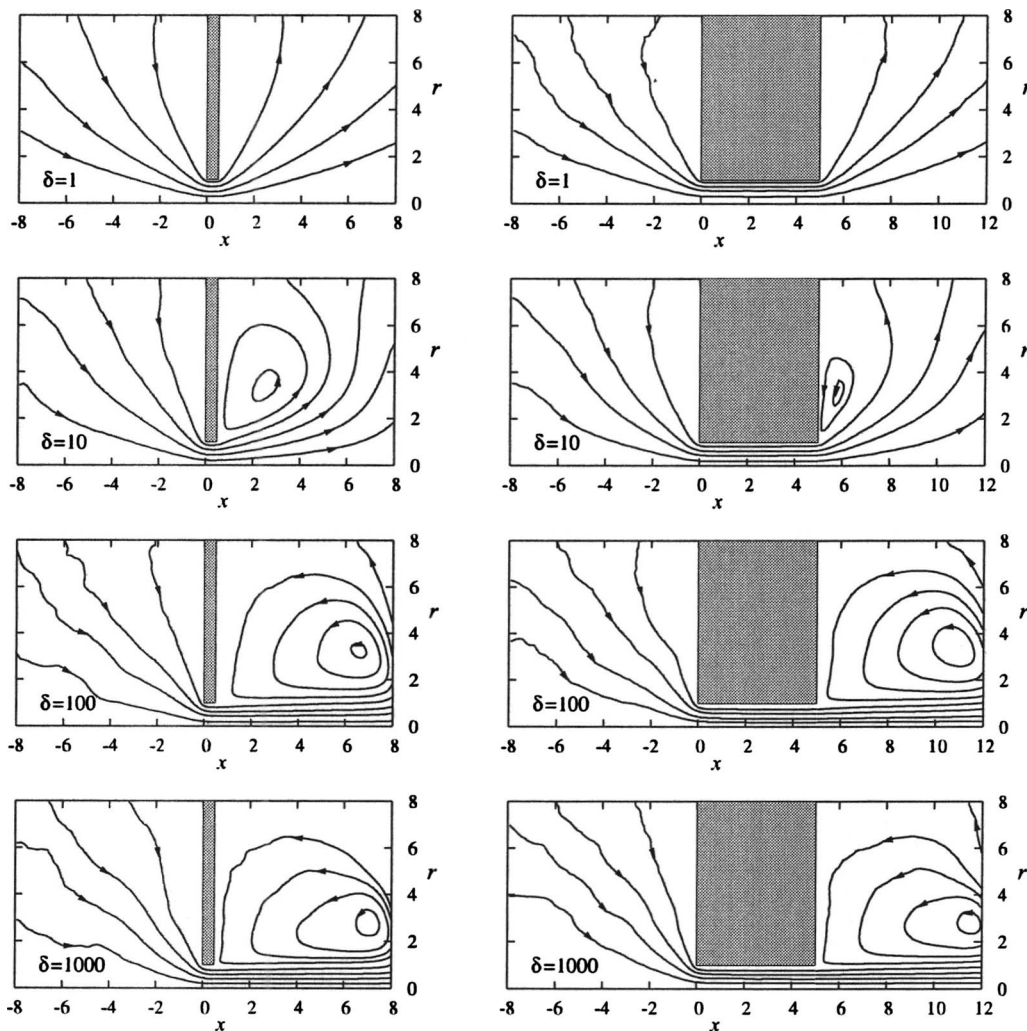| P_1/P_0	δ	$L/R=0.1$	1	5
		W		
0.2	1	0.889	0.622	0.269
	10	1.35	1.02	0.507
	100	1.49	1.35	1.06
	1000	1.51	1.45	1.26
	2000	1.51	1.46	1.27
0.3	1	0.790	0.552	0.242
	10	1.30	0.989	0.477
	100	1.47	1.35	1.05
	1000	1.49	1.45	1.27
	2000	1.49	1.45	1.25
0.4	1	0.689	0.480	0.208
	10	1.24	0.937	0.437
	100	1.43	1.33	1.031
	1000	1.45	1.43	1.22
	2000	1.45	1.43	1.23

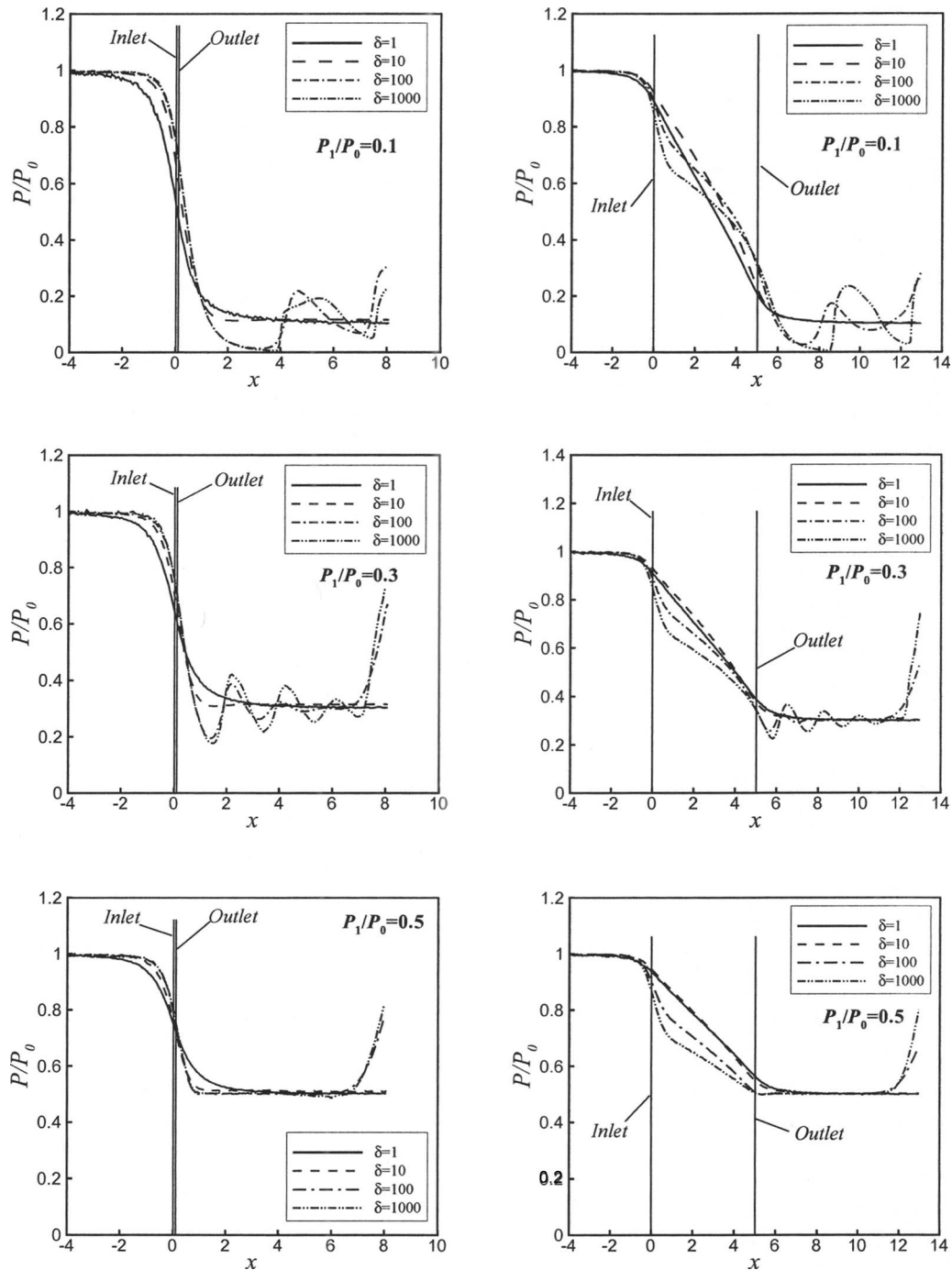FIG. 7. Streamlines for various δ, with $P_1/P_0=0.5$ and $L/R=0.5$ (left) and $L/R=5$ (right).

FIG. 8. Pressure distributions along $r=0$ for various δ and P_1/P_0 with $L/R=0.1$ (left) and $L/R=5$ (right).

for $\delta=1$, is small and it is reduced as the pressure and the length-to-radius ratios are increased. The pressure and temperature variations for $\delta=1$ and 10 are qualitatively similar.

For $\delta=10^2$, both pressure and temperature variations, compared to those for $\delta=1$ are drastically changed, i.e., they are not monotonic anymore. In Fig. 8, for $\delta=10^2$, the pressure at the exit of the tube is reduced well below P_1/P_0 and then along the distance $L/R<x\leqslant L/R+8$, it is characterized by an oscillatory behavior with reducing amplitude around its downstream equilibrium value. Such a phenomenon is called Mach disks and has been earlier discussed in slightly

rarefied gas flows using a quasi-gas-dynamics approach.[21,22] The oscillatory behavior is reduced as the pressure ratio is increased and finally it vanishes at $P_1/P_0=0.5$. This oscillatory behavior of the pressure is due to the compression waves, which are produced inside the tube and they propagate downstream. The corresponding behavior of the temperature variation, in Fig. 9, for $\delta=10^2$, has similar characteristics with the ones for pressure. Also, the pressure and temperature variations for $\delta=10^3$ are qualitatively similar to the one for $\delta=10^2$. Comparing all temperature variations in terms of δ, it is seen that the minimum values of the tem-
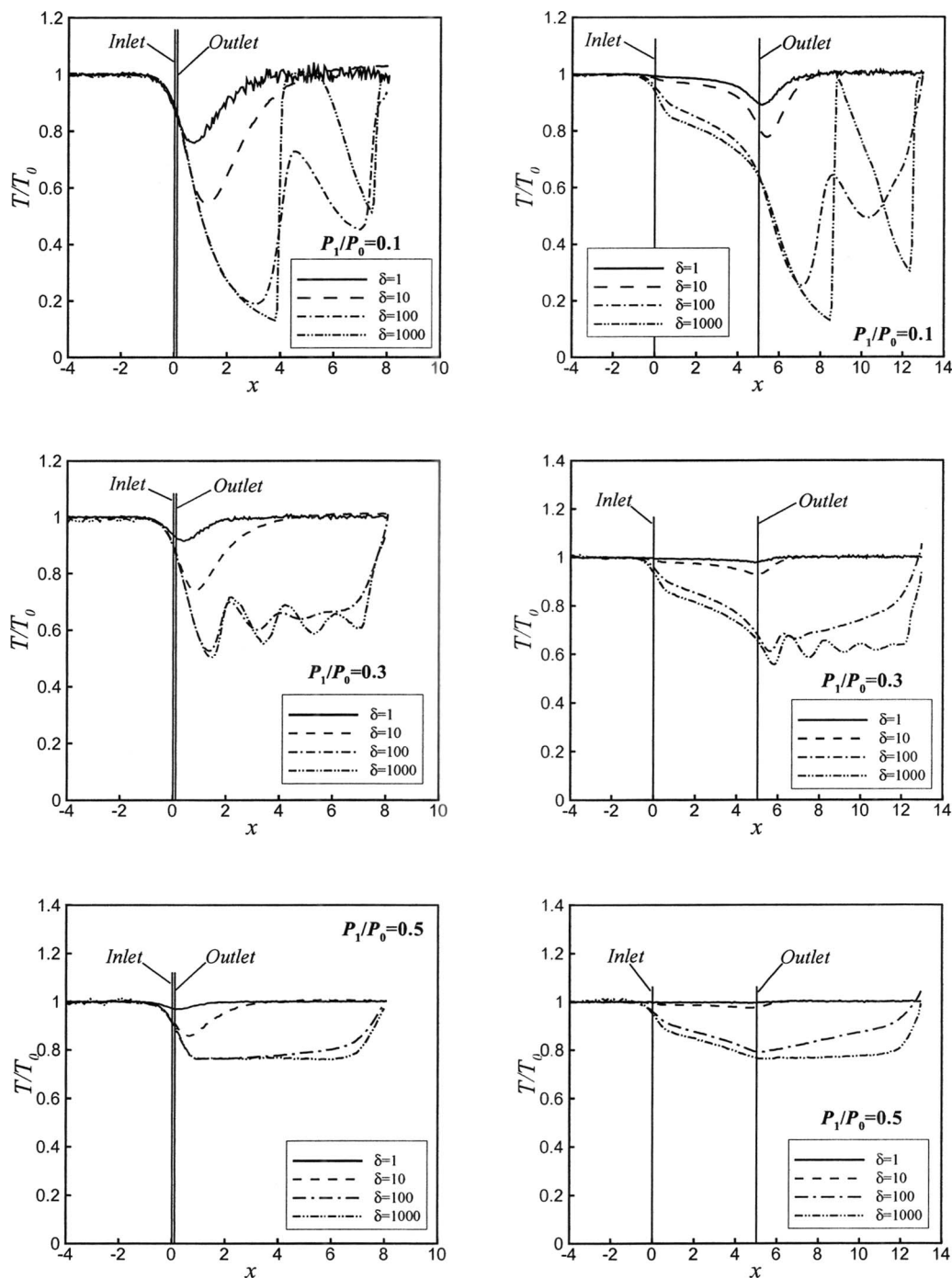
FIG. 9. Temperature distributions along $r=0$ for various δ and P_1/P_0 with $L/R=0.1$ (left) and $L/R=5$ (right).

perature departure from equilibrium is increased as the rarefaction is decreased (i.e., as δ is increased). It is also noted that the pressure and temperature variations do not change significantly in terms of L/R. As a general remark, it is stated, that the pressure and temperature fields (and therefore the whole flow field) depend strongly on P_1/P_0 as well as on δ, while their dependency on L/R is not as strong.

The variation in the Mach number along $r=0$ is shown in Fig. 10. For a monoatomic gas the local Mach number is computed from the gas velocity according to Ma $=\sqrt{6T_0/5Tu_x}/v_0$. Far upstream, the Mach number is equal to

zero. Then, at the same point (about $x=-2$), where the pressure starts to decrease, the Mach number starts to increase. It keeps increasing along the tube and it reaches its maximum value, which, as it is seen, strongly depends on P_1/P_0 and δ, while it is practically independent of L/R, at the exit of the tube. Then, it starts decreasing toward zero. It is seen that for the same pressure ratio, as δ is decreased, the maximum value of the Mach number is drastically decreased, too. For sufficiently low pressure ratio, the flow may be supersonic at the exit of the tube when $\delta=10^2, 10^3$, but it becomes subsonic when $\delta=1, 10$. Also, for the same pressure ratio, as the
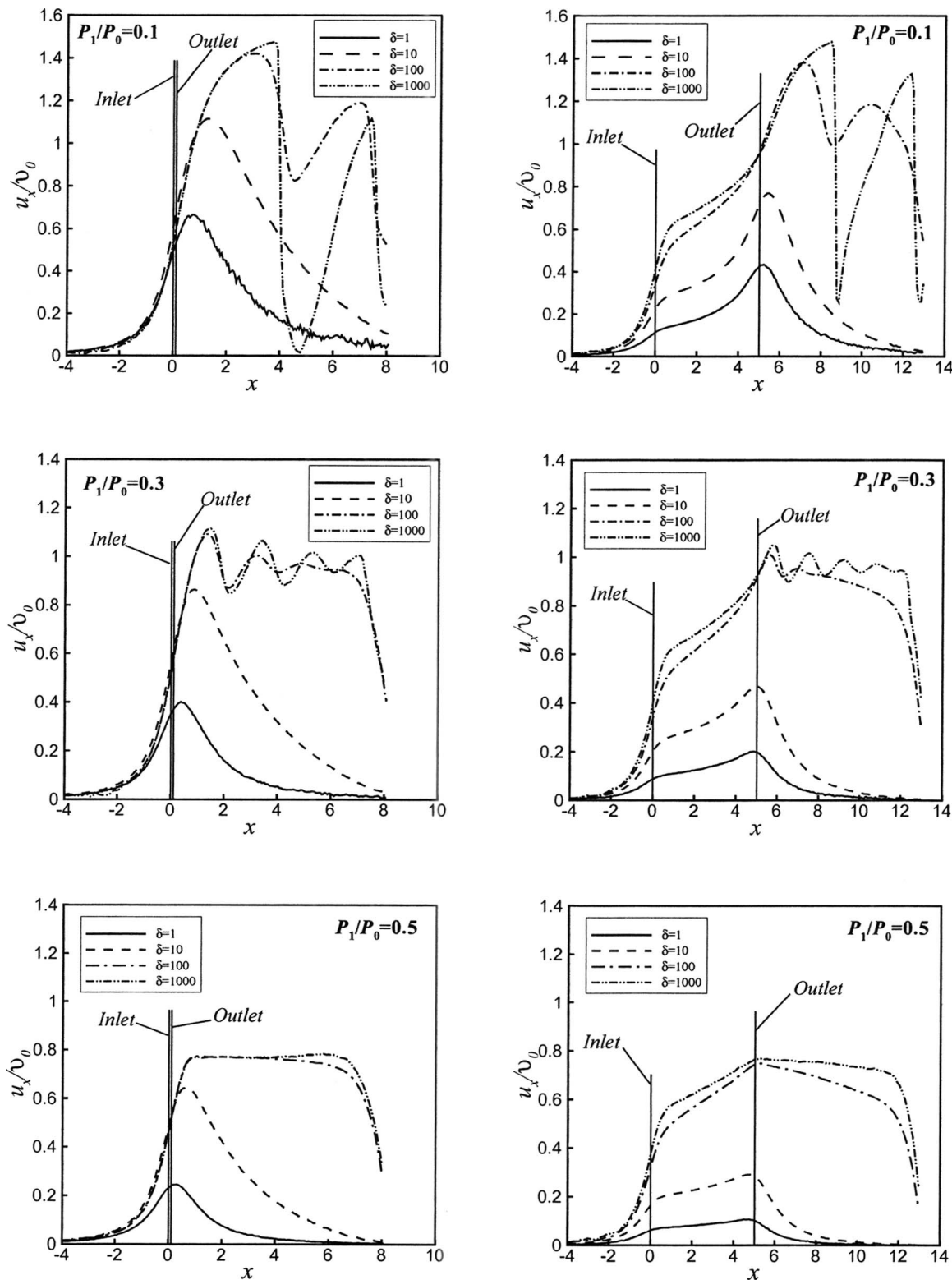
FIG. 10. Axial velocity distribution along $r=0$ for various δ and P_1/P_0 with $L/R=0.1$ (left) and $L/R=5$ (right).

rarefaction parameter is decreased, the oscillatory behavior of the Mach number at the downstream reservoir is reduced and finally vanishes. These observations are in agreement with the reported flow rates in Sec. IV A.

Next, in order to observe in a more detailed manner the flow field characteristics inside the tube, the velocity, pressure, and temperature profiles are plotted at the inlet $(x=0)$, middle $(x=L/(2R))$, and outlet $(x=L/R)$ of a tube with
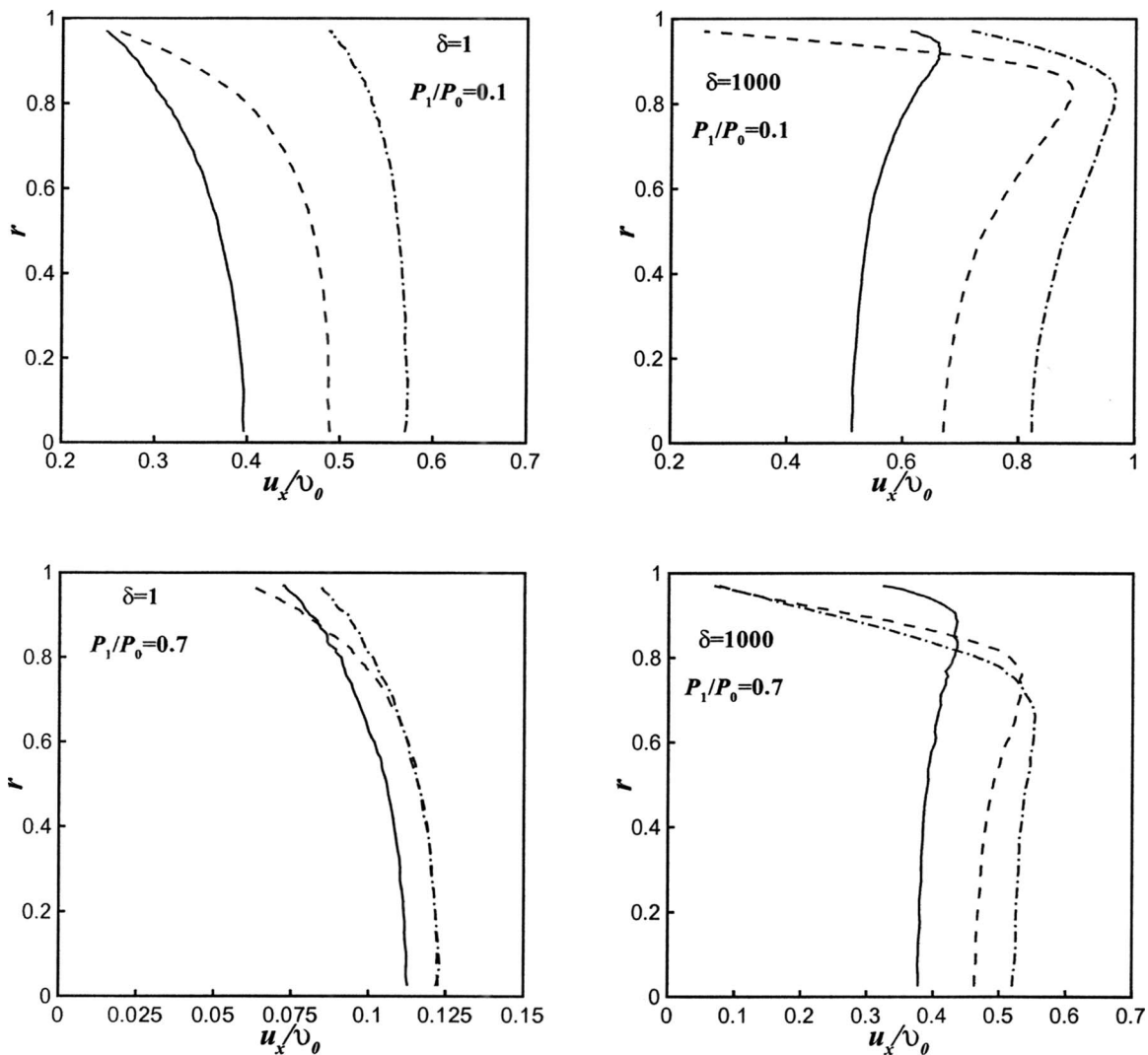
FIG. 11. Velocity profiles at the inlet ($x=0$: __), middle ($x=L/(2R)$: – – –) and outlet ($x=L/R$: –·––·–) cross sections of a tube with $L/R=0.5$.

$L/R=0.5$, $\delta=1,10^3$, and $P_1/P_0=0.1,0.7$. The selected combinations of δ and P_1/P_0 may be considered as indicative for cases when both of them are small or large, as well as for cases when one of them is small and the other is large and the presented radial profiles may be considered as typical for the flow evolution along the tube.

Starting with the velocity profiles u_x, shown in Fig. 11, the way that the flow is accelerated from one cross section to the next one is clearly demonstrated. The acceleration becomes faster as P_1/P_0 is decreased and δ is increased. At $\delta=1$ and $P_1/P_0=0.7$, the acceleration of the flow is negligible. The shape of the corresponding profiles for $\delta=1$ and $\delta=10^3$ is quite different. For $\delta=1$, the profiles follow a parabolic type shape having minimum and maximum values at the wall and at the center of the tube, respectively. For $\delta=10^3$, the velocity profiles reach their maximum values near the wall, at $r \simeq 0.8$ and not in the center of the tube as it might be expected. This behavior occurs both for $P_1/P_0=0.1$ and 0.7,

but it becomes clearer at small pressure ratios (i.e., at large pressure drops).

The corresponding pressure $P(x)$ and temperature $T(x)$ profiles are shown in Figs. 12 and 13, respectively. For each set of parameters, the pressure and temperature drop in the tube may be observed. For $\delta=1$ it is seen that the slope of the pressure profiles at the inlet and outlet cross sections is opposite (i.e., at $x=0$ the pressure is higher close to the wall than at the center of the tube and at $x=L/R$ is the other way around), while in the middle cross section $x=L/2R$, the pressure is almost constant. For $\delta=10^3$, the pressure profiles have at the inlet a parabolic type shape, which is flattening gradually along the tube. The shape of the corresponding temperature and velocity profiles possess an antisymmetric qualitative resemblance. The locations in the tube with high velocities are characterized by low temperatures and vice versa. Also, for $\delta=1$ in all three cross sections, the temperature at the center of the tube is lower than close to the walls,
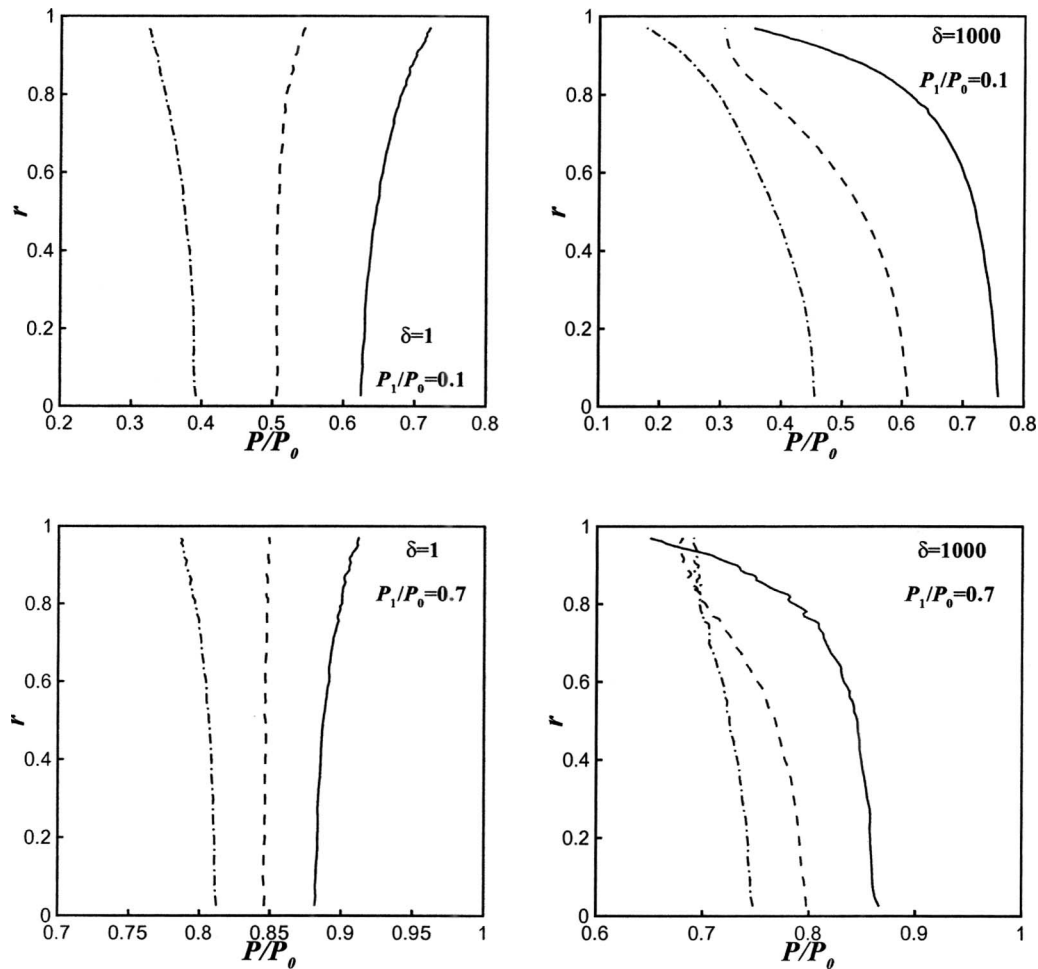
FIG. 12. Pressure profiles at the inlet ($x=0$: ___), middle ($x=L/(2R)$: $-\,-\,-$) and outlet ($x=L/R$: $-\cdot-\cdot-$) cross sections of a tube with $L/R=0.5$.

while for $\delta=10^3$, the temperature profiles have a minimum at $r\simeq0.8$. At $\delta=1$ and $P_1/P_0=0.7$, the temperature variation inside the tube is negligible and the flow is almost isothermal. The presented results in Figs. 11–13 for $L/R=0.5$ are indicative for all length-to-radius ratios.

Finally, for a complete view of the whole flow field, the isolines of the local Mach number are plotted in Fig. 14, covering the region around and inside the tube for $L/R=0.5$, $\delta=1, 10^2$, and $P_1/P_0=0.1, 0.7$. It is seen that for the same pressure ratios, the flow fields downstream from the exit of the tube vary significantly both qualitatively and quantitatively between $\delta=1$ and $\delta=10^2$. It is also seen that the effect of various P_1/P_0 is more significant in dense rather than in rarefied conditions. Based on the results presented in this subsection, it may be argued that rarefaction has the most significant effect on the flow characteristics and patterns, followed by the pressure ratio drop, while the length-to-radius ratio has a rather modest impact.

V. CONCLUDING REMARKS

The rarefied gas flow through circular tubes of finite length has been investigated computationally in terms of the three parameters defining the flow problem, namely, the rar-

efaction parameter δ, the length-to-radius ratio L/R, and the pressure ratio P_1/P_0. The numerical scheme is based on the DSMC method. Results are presented for the first time, in tabulated and graphical forms, for the flow rate, the bulk distributions of velocity, pressure and temperature, and the Mach number for the following range of the main parameters: $0\leqslant\delta\leqslant2000$, $0\leqslant L/R\leqslant10$, and $0\leqslant P_1/P_0\leqslant0.7$. For some specific flow configurations, the numerical results are found to be in very good agreement with available experimental results. Since the presented results correspond to a wide range of the all three involved parameters, their effect on the flow patterns and characteristics has been examined in a detailed and systematic manner.

It has been shown that the flow quantities and characteristics strongly depend on δ and P_1/P_0, while their dependency on L/R is not as strong. As a qualitative remark, it may be stated that as δ is decreased and intermolecular collisions become rare, the strength of the vortex creating mechanisms is reduced, and the flow view is gradually simplified. Also, the decrease in P_1/P_0 (i.e., the increase in the pressure drop) in rarefied atmospheres alters the flow quantities but not the flow patterns, while in dense atmospheres, it has both a qualitative and a quantitative impact. In addition,
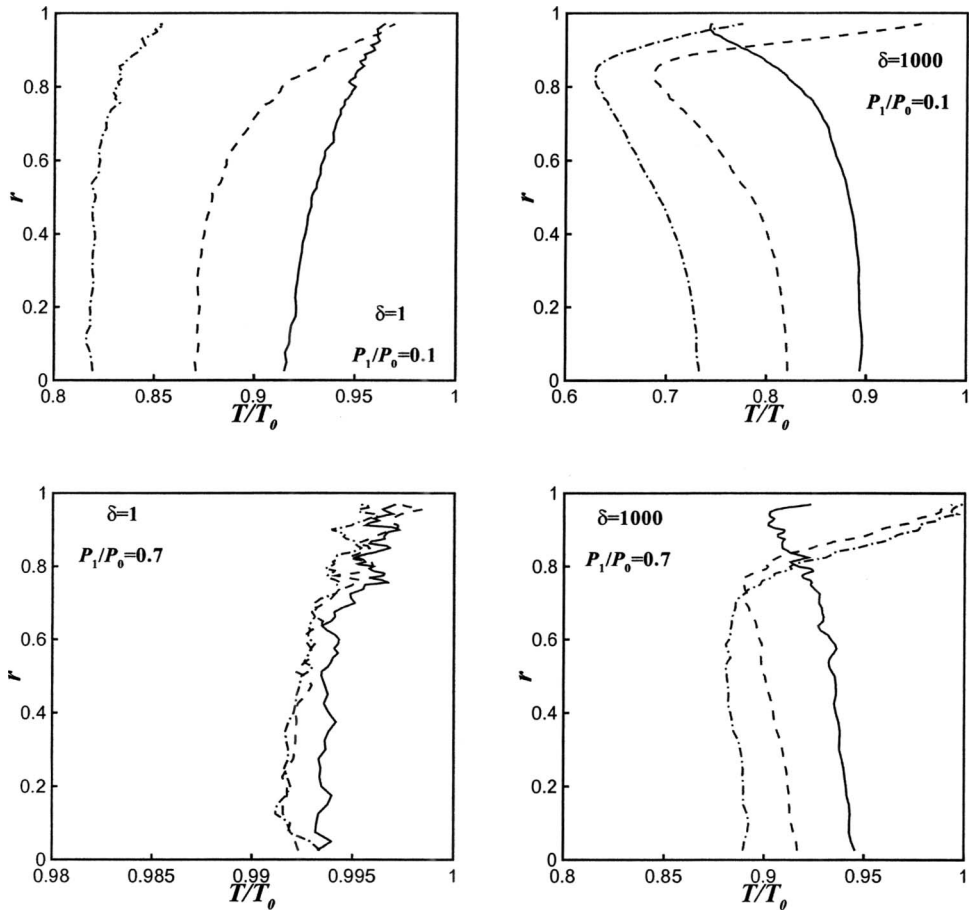
FIG. 13. Temperature profiles at the inlet ($x=0$: ___), middle ($x=L/(2R)$: – – –) and outlet ($x=L/R$: –·–·–) cross sections of a tube with $L/R=0.5$.
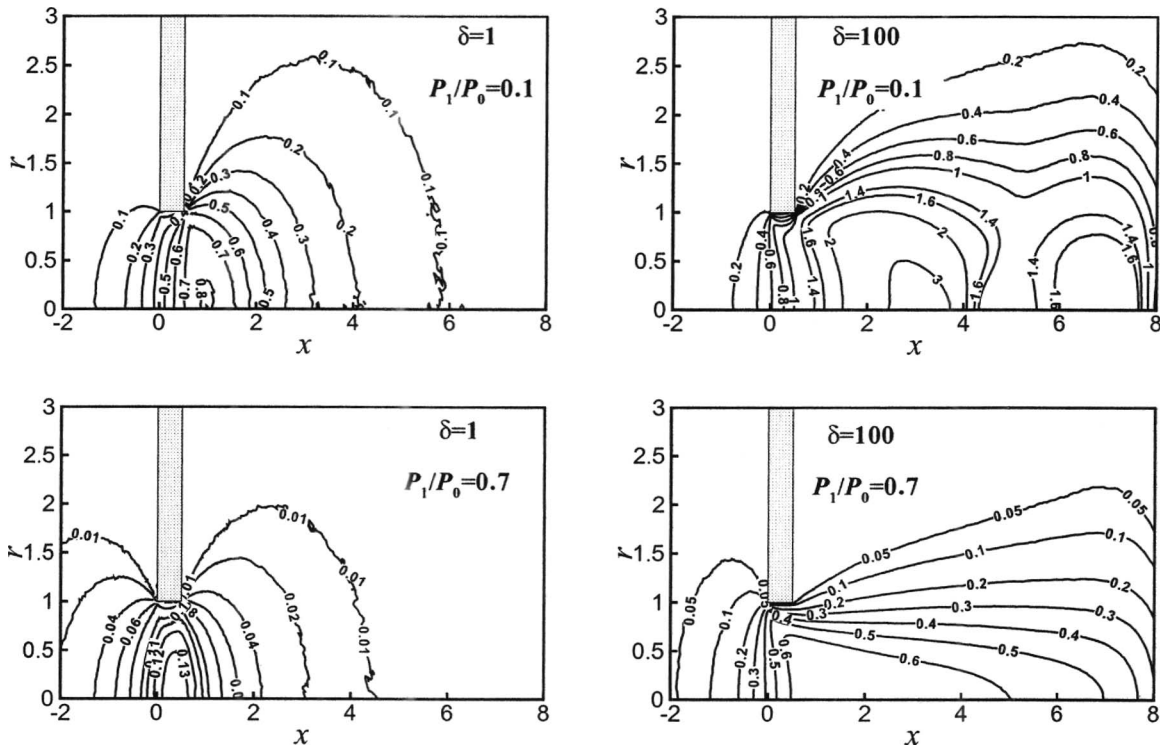

FIG. 14. Isolines of local Mach number for typical values of δ, P_1/P_0 and $L/R=0.5$.

several interesting findings have been reported including the behavior of the flow rate and other macroscopic quantities in terms of the three basic problem parameters, while the issues of the choked flow and of the Mach disks at large pressure drops have been discussed.

The present results could be useful to plan experimental works as well as to design and optimize systems operating under low pressure conditions or microfluidics devices.

ACKNOWLEDGMENTS

[1] M. Knudsen, Ann. Phys. (N.Y.) **28**, 999 (1909).
[2] P. Clausing, J. Vac. Sci. Technol. **8**, 636 (1971).
[3] R. Hanks and H. Weissberg, J. Appl. Phys. **35**, 142 (1964).
[4] A. K. Sreekanth, Phys. Fluids **8**, 1951 (1965).
[5] B. T. Porodnov, P. E. Suetin, S. F. Borisov, and V. D. Akinshin, J. Fluid Mech. **64**, 417 (1974).
[6] T. Fujimoto and M. Usami, ASME Trans. J. Fluids Eng. **106**, 367 (1984).
[7] F. Sharipov, J. Fluid Mech. **518**, 35 (2004).
[8] F. Sharipov and V. Seleznev, J. Phys. Chem. Ref. Data **27**, 657 (1998).
[9] *Handbook of Vacuum Technology*, edited by K. Jousten (Wiley-VCH Verlag, Weinheim, 2008).
[10] F. Sharipov, *Encyclopedia of Microfluidics and Nanofluidics*, D. Li (Springer-Verlag, New York, 2008), pp. 772–778.
[11] G. A. Bird, *Molecular Gas Dynamics and the Direct Simulation of Gas Flows* (Oxford University Press, Oxford, 1994).
[12] H. Shinagawa, H. Setyawan, T. Asai, Y. Sugiyama, and K. Okuyama, Chem. Eng. Sci. **57**, 4027 (2002).
[13] M. Usami and K. Okuyama, JSME Int. J., Ser. B **42**, 369 (1999).
[14] G. Koppenwallner, T. Lips, and C. Dankert, in *Rarefied Gas Dynamics*, edited by M. S. Ivanov and A. K. Rebrov (Siberian Branch of the Russian Academy of Science, Novosibirsk, 2007), pp. 585–591.
[15] S. F. Gimelshein, G. N. Markelov, T. C. Lilly, N. P. Selden, and A. D. Ketsdever, in *Rarefied Gas Dynamics*, edited by M. Capitelli (American Institute of Physics, Melville, NY, 2004), pp. 437–443.
[16] T. Lilly, S. Gimelshein, A. Ketsdever, and G. N. Markelov, Phys. Fluids **18**, 093601 (2006).
[17] S. Varoutis, D. Valougeorgis, O. Sazhin, and F. Sharipov, J. Vac. Sci. Technol. A **26**, 228 (2008).
[18] L. Marino, Microfluid. Nanofluid. **6**, 109 (2009).
[19] W. Wagner, J. Stat. Phys. **66**, 1011 (1992).
[20] W. Jitschin, U. Weber, and H. K. Hartmann, Vacuum **46**, 821 (1995).
[21] B. Maté, I. A. Graur, T. Elizarova, I. Chirokov, G. Tejeda, J. M. Fernández, and S. Montero, J. Fluid Mech. **426**, 177 (2001).
[22] I. A. Graur, T. G. Elizarova, A. Ramos, G. Tejeda, J. M. Fernández, and S. Montero, J. Fluid Mech. **504**, 239 (2004).